International Journal of Coal Geology 180 (2017) 100–112

Contents lists available at ScienceDirect

International Journal of Coal Geology

journal homepage: www.elsevier.com/locate/coal

Multi-scale 3D characterisation of porosity and organic matter in shales with variable TOC content and thermal maturity: Examples from the Lublin and Baltic Basins, Poland and Lithuania

Lin Ma[a,b,d,*], Kevin G. Taylor[a], Patrick J. Dowey[a], Loic Courtois[b,c,d], Ali Gholinia[d], Peter D. Lee[b,c,d]

[a] School of Earth and Environmental Sciences, University of Manchester, Manchester M13 9WJ, UK
[b] Manchester X-ray Imaging Facility, School of Materials, University of Manchester, Manchester M13 9PJ, UK
[c] Research Complex at Harwell, Rutherford Appleton Laboratory, Harwell, Oxfordshire OX11 0FA, UK
[d] School of Materials, University of Manchester, Manchester M13 9PJ, UK

ARTICLE INFO

Keywords:
Organic matter geometry
Organic matter network
Pore types
Pore distribution
TOC
Maturity
X-ray tomography
FIB-SEM

ABSTRACT

Understanding the distribution of pores and organic matter with varying organic matter concentrations and maturity is essential to understanding fluid flow in shale systems. Analysis of samples with low, medium, and high total organic carbon (TOC) and varying maturities (gas-mature and oil-mature) enables the impact of both organic matter concentrations and thermal maturation on organic matter porosity to be examined. Three gas-mature samples of varying TOC (Lublin Basin) and one oil-mature sample (Baltic Basin), both with similar mineral compositions, were selected from the same formation. Samples were imaged in 3D over four orders of magnitudes (pixel sizes from 44 μm to 5 nm). A combination of X-ray computed tomography (XCT) and Focus Ion Beam Scanning Electron Microscopy (FIB-SEM) enabled the morphologic and topological characteristics of minerals, organic matter and pores to be imaged and quantified.

In the studied samples, organic matter primarily has two geometries: lamellar masses (length: 1–100 μm, thickness: 0.5–2.0 μm) and discrete spheroidal particles (0.5–20.0 μm). Organic matter forms an inter-connected network where it exceeds a concentration between 6 and 18 wt%.

Different pore types have different diameters and total pore volumes: inter-mineral pores (0.2 μm, 10–94%), organic interface pores (0.2 μm, 2–77%), intra-organic pores (0.05 μm, 1–40%) and intra-mineral pores (0.05 μm diameter, 1–2% of total porosity). The major pore system in the studied shales is composed of inter-mineral pores which occur between clay mineral grains. TOC concentration influences the total volume of organic matter-related pores while maturity controls the presence of intra-organic pores. The study improves the understanding of the relationship of organic matter concentrations, maturity and pore systems in shales. This study characterises porosity and organic matter distributions in 3D; it also improves the understanding of the relationship of organic matter concentrations, maturity and pore systems in shales.

1. Introduction

Technological advances in horizontal drilling and hydraulic fracturing have paved the way for the exploration and production of shale gas and shale oil. Shale reservoirs are organic-rich (> 2% TOC) and have an extremely low permeability of between 1 μD and 1 nD (Britt, 2012; Clarkson et al., 2012; Macbeth et al., 2011). In these self-contained source-reservoir shale systems, the nature and characteristics of organic matter and pores are two critical factors influencing the generation, storage and transport of hydrocarbons.

Organic matter morphology and structure can vary on a micron to sub-micron scale (Curtis et al., 2014) and the extent and connectivity of organic matter has been reported to affect both storage capacity and permeability in shales (Curtis et al., 2014). This is due to the perceived importance of organic matter-related pores and the gas sorption and diffusion properties of organic matter (Curtis et al., 2014; Sondergeld et al., 2013). The majority of organic macerals and pores within shales are on the sub-micron to nano-scale (Loucks et al., 2012; Ma et al., 2016, 2017). The volume and sizes vary with components, microstructures, and sometimes, maturities (Curtis et al., 2011; Kuila et al.,

* Corresponding author.
E-mail address: lin.ma@manchester.ac.uk (L. Ma).

http://dx.doi.org/10.1016/j.coal.2017.08.002
Received 25 June 2017; Received in revised form 4 August 2017; Accepted 5 August 2017
Available online 07 August 2017

2012). The small sizes of these components coupled with the highly heterogeneous nature of shales make imaging and accurate quantification of pore and organic structures challenging.

Traditional studies focussing on the distribution of organic matter in 2D using optical microscope and scanning electron microscopy (SEM) techniques (Bocangel et al., 2013; Curtis et al., 2014; Sondergeld et al., 2013) do not provide information on the 3D spatial distribution and connectivity of organic matter and pores, which is essential to accurately characterise these phases. More recently, integrated 2D and 3D imaging studies of organic matter porosity in shales of varying maturity or mineral-associated porosity in shales of varied mineral compositions have been undertaken, and have documented the importance of this approach. However these studies (Klaver et al., 2015; Loucks et al., 2012) have tended to incorporate only high resolution datasets of small volumes (Ambrose et al., 2010; Curtis et al., 2012b; Ma et al., 2015).

X-ray computed tomography (XCT) and focused ion beam scanning electron microscope (FIB-SEM) techniques have been shown to provide quantitative 3D datasets and have recently been applied to a range of shales. In combination, these techniques enable shale compositions to be characterized in 3D across multiple scales (mm-nm) (Heath et al., 2011; Sakellariou et al., 2003; Wang and Reed, 2009). However, because pores in shales can occur at the nm scale (Ambrose et al., 2010; Bai et al., 2013; Curtis et al., 2010), the full range of pores cannot be imaged using XCT and FIB-SEM techniques alone. Porosity studies based on nitrogen adsorption (Labani et al., 2013; Liu et al., 2015) can accurately measure bulk effective porosity over a fuller range of pore scales, but do not provide detailed information on pore morphology. The application of both bulk porosity measurements and 3D multiscale imaging ensures that the range of porosity types, sizes and morphology can be quantified (Ma et al., 2016).

Here we primarily investigate the variability in variation of organic matter geometry and connectivity and porosity form, size and connectivity in gas-mature shales with a wide range of TOC contents. Secondly, we compare observations from these gas-mature shales to analogous shales that are only oil-mature. To characterise the morphological, size and spatial variability of organic matter and pore systems within these shales, 3D imaging techniques including XCT and FIB-SEM and 2D imaging techniques including optical microscope and SEM were performed in this study, and integrated with nitrogen adsorption and helium porosimetry. These data and associated discussion enable a greater understanding on the controlling factors of organic matter distribution, pore systems and fluid flow in these complex rocks.

2. Sample selection and geological setting

Three gas-mature samples with high, medium and low organic carbon contents and one oil-mature sample with high organic carbon were selected from two subsurface cores in the Llandovery-Wenlock series (Lower Silurian) shale formation of the Lublin and Baltic Basins in Poland and Lithuania, respectively (Fig. 1). The samples were provided by Chevron with specification of the play location, but not of the exact core location and depth. The samples were selected on the basis of their similar mineral composition and texture. Both basins had a similar depositional history controlled by a relatively simple structural settings (Karcz et al., 2013; Nawrocki and Poprawa, 2010) making comparison between samples and wells appropriate.

The Baltic-Lublin Basins formed a flexural foredeep during the Caledonian collision in the late Ordovician and Silurian (Poprawa et al., 1999). Flexural subsidence and low detrital input during early basin-filling produced both accommodation space and anoxic conditions; this enabled the development of organic-rich shale. Sediments of Llandovery-Wenlock are dominated by graptolite shales, marlstone and fine-grained limestones, the latter locally comprise deep- to shallow-marine carbonates (Zdanaviciute and Lazauskiene, 2007).

The sedimentary sequence in these basins contains several marine-shale deposits which in places are 300–820 m thick, have an average TOC of 3.9% and are buried at prospective depths of 1000 to 5000 m (Jędrzejczyk et al., 2014). Major subsidence in the early Paleozoic caused complex lateral variability in burial depth of the Silurian shale between 1000 m and 3500 m with maximum local changes in SW and minimum in NE (EIA, 2011). In the southeast of the Lublin Basin, Poland, Lower Silurian shales reached the gas window in Late Paleozoic (Karcz et al., 2013), while in the Baltic basin (Lithuania), Lower Silurian shales only reached the oil generation window. Both basins are potential shale gas or shale oil plays attracting recent exploration actives (EIA, 2011; Zdanaviciute and Lazauskiene, 2007) with the estimated recoverable shale gas and oil resources of 346–768 Bcm (PGI, 2012).

Present-day TOC values (see methods) for three selected gas-mature samples L1, L2 and L3 in the Lublin Basin (Poland) were 9 wt%, 4 wt%, 1 wt% and for oil-mature sample B1 in the Baltic Basin (Lithuania) TOC was 10 wt%. Thermal maturity values (Ro) are around 2.2% for the Lublin Basin samples and 0.8% for the Baltic sample.

3. Methods

3.1. Physical and chemical analyses

Optical microscopy and scanning electron microscopy (SEM; XL30 Environmental SEM, FEI) with energy-dispersive X-ray spectroscopy (EDX) were used to analyse the petrological, mineralogical and textural characteristics of all samples. Thin sections were prepared and the surfaces were polished with a 0.25 μm abrasive for SEM observation. X-ray diffraction analysis (D8Advance XRD, Bruker) was performed on whole rock samples to confirm the mineral phases comparing experimental peaks to ICDD (International Centre for Diffraction Data) database. Mineral quantification was carried out using Topas version 4.2 for all four samples, and has a volume error ± 1%. TOC was measured using a Leco carbon analyser at the University of Newcastle. Samples underwent acidification followed by organic matter combustion. The calculated error for this technique is ± 0.02%. Proprietary vitrinite reflectance (%Ro) values were provided by Chevron.

Bulk porosity of samples was obtained on 15–25 mm diameter cylinders using a helium (He) porosimeter (ResLab) with an error of ± 0.1%. To validate image-based pore quantification, pore-size distributions were measured using nitrogen sorption techniques on a surface area analyser (ASAP 2020, Micromeritics). This was performed with increasing nitrogen (N_2) pressure for adsorption and decreasing pressure for desorption at a temperature of 77 K. The data was collected to establish a hysteresis loop and analysed using Brunauer-Emmett-Teller (BET) theory (Brunauer et al., 1938). The pore volumes and sizes were calculated using the Barrett-Joyner-Halenda (BJH) method (Barrett et al., 1951). Due to the required degassing of samples prior to N_2 low-pressure sorption, pore structure data was reported on the same dry basis as helium porosimetery.

3.2. Imaging techniques

3.2.1. X-ray tomography (meso- to micro-scale)

X-ray tomography images of the samples were generated by acquiring a series of 2D 'projections' where each projection is a radiographic image collected from a different angle. The sample is placed in the X-ray beam and rotated 360° around a vertical axis collecting images at regular intervals. As each mineral phase has specific X-ray absorption characteristics and because the sample rotates, the mineral assemblage along the beam path varies. During sample rotation, because of this variation the total X-ray flux hitting each pixel on the detector varies (Hsieh, 2009; Ketcham and Carlson, 2001; Long et al., 2009; Wellington and Vinegar, 1987). Mathematical reconstruction algorithms are then applied to reconstruct a 3D absorption (density/mineralogy) maps. The data presented here were collected at the Manchester X-ray Imaging Facility (MXIF) at the University of

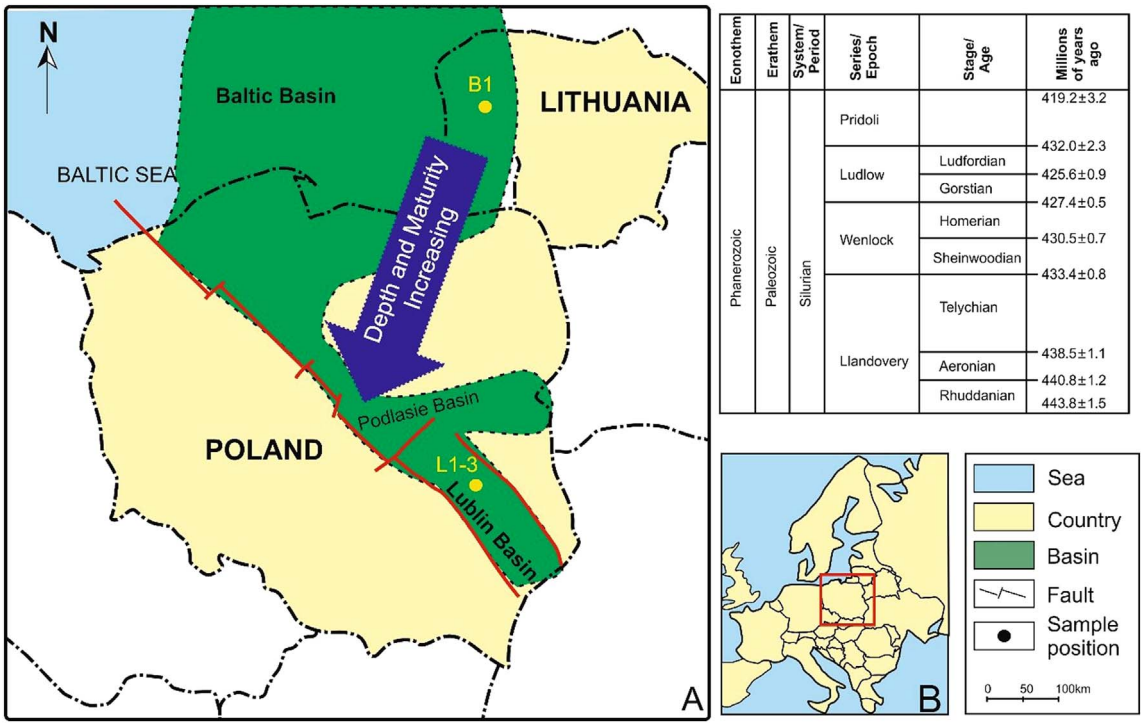

Fig. 1. Geological map with sample locations (EIA, 2013). (A) Map of Europe with the locations of the Lublin and Baltic Basins. (B) Sample location L1-3 in the Lublin Basin, Poland and sample location B1-3 in the Baltic Basin, Lithuania.

Table 1
Characteristics of each imaging scale in this study and facility used.

Abbreviation	Scales	Sample size	Pixel size (μm) X Y Z	Facility used
R1	Meso	6 cm	44.4 × 44.4 × 44.4	Nikon XT H 225
R2	Micro	1 mm	0.494 × 0.494 × 0.494	I13 Beamline at Diamond Light Source
R3	Sub-micron	65 μm	0.128 × 0.128 × 0.128	Zeiss Xradia Ultra Nano CT
R4	Low-resolution nano scale	15 μm	0.005 × 0.005 × 0.2	FEI Nova 600i FIB-SEM
R5	High-resolution nano scale	5 μm	0.005 × 0.005 × 0.05	FEI Nova 600i FIB-SEM

Manchester, and at the Diamond Light Source (DLS) synchrotron. The mesoscale samples (5 cm cube; resolution referred to as R1 throughout) were imaged with a spatial resolution of 44 μm/voxel (a 3D equivalent of a pixel and the smallest unit of a volume data set) using X-ray tomography system (XT H 225, Nikon, Tokyo, Japan, Table 1). All scales and resolutions are consistent with previous studies in Bowland shale (Ma et al., 2016). The image datasets at R1 cannot provide sufficient evident for organic matter and pores therefore not present in this study. The microscale samples (approximately 1 mm diameter; resolution = R2) were imaged on the Diamond-Manchester Beamline (Diamond Light Source, Oxfordshire, United Kingdom) with voxel resolutions of 0.5 μm. Sub-micron scale samples (~65 μm diameter; resolution = R3) were imaged using a laboratory nano-tomography system (Xradia Ultra, Zeiss, Oberkochen, Germany) with a voxel resolution of ~0.12 μm. All these samples were prepared using the wire saw in rock deformation lab, University of Manchester.

3.2.2. FIB–SEM (nano-scale)

A dual beam FIB (Nova 600i, FEI) was used to collect nano-scale images of samples. This technique utilises a gallium ion beam and an electron beam in the SEM (Ghous et al., 2008; Martínez et al., 2008; Zhang et al., 2011). The ion beam is used to mill material from the shale surface by sputtering away a volume of the sample via momentum transfer. In situ 2D SEM images of the newly milled shale surface are collected after each milling step. The extremely high precision of milling by the ion beam and SEM imaging allows the collection of 3D datasets at the nano scale. Hundreds of SEM images of samples were acquired with resolutions of ~10 nm by 10 nm (resolution = R4) or ~5 nm by 5 nm (resolution = R5) with vertical 2D slice spacings of ~200 nm and ~50 nm respectively.

Because of issues with FIB-SEM imaging and representativity (Kelly et al., 2016; Ma et al., 2017), care was taken to ensure that sample sites were as representative as possible. Sample sites were selected after observation of the entire sample (3 × 2 cm^2) in the SEM, and sites were selected that represented the variability in texture and compositions observed in the sample. Organic-rich, clay mineral-rich, and granular mineral-rich sites were chosen to cover this variability.

3.2.3. Image processing and quantification

Distinct phases were quantified using filtered and segmented images (Stauber and Müller 2008; Korfiatis et al., 2007; Landis and Keane, 2010). The filters applied for de-noising include: a non-local means filter (Buades et al., 2005) (parameters: local neighbourhood pixel 5 and similarity value 0.3), a median filter (Brownrigg, 1984) (parameters: kernel size 3), a sobel filter (Kanopoulos et al., 1988) (parameters: two 3 × 3 kernels - one for horizontal changes, and one for vertical) and an edge-preserving smoothing filter (Nagao and Matsuyama, 1979) (parameters: contrast 5, sigma 2). The 3D and 2D versions of the filters were applied to both 3D and 2D images. Organic matter and pores were identified by grey values and labelled by

Table 2
Measurements and calculations used to quantify the physical and morphological characteristics of pores and organic matter.

Measurement	Definition
Length	Maximum length of the pores in 3D, μm
Width	Minimum length of the pores in 3D, μm
Volume	Volume of individual pores, μm^3
Surface area	Surface of individual pores, μm^2
Equivalent diameter	Equivalent diameter of individual pores was calculated as the equivalent circular diameter to represent the pore size, $\sqrt[3]{\frac{6}{\pi}V}$, μm
Elongation	The ratio of the maximum length and minimum length of pores, Length/width
Orientation	The angle between the long axis and bedding plane, degrees
Distance	The shortest edge to edge distance from the current object to its nearest neighbour, μm
Local thickness	The diameter of the largest sphere that fits inside the object, μm
Nearest neighbour distance	The distance between the pore and its nearest neighbour, $\sqrt{(X_i - X_i)^2 + (Y_i - Y_i)^2 + (Z_i - Z_i)^2}$, μm

independence and the surface area, volume, orientation, length and width of individual pore/organic matter particles were measured in voxels using Avizo software (Standard and Fire versions, FEI). From these measurements the equivalent diameter, elongation, distance, local thickness and nearest neighbour distance were calculated based on the equations in Table 2.

4. Results

4.1. Mineralogy

XRD analyses indicate that the samples are composed of quartz, muscovite, chlorite, albite, calcite, dolomite, and pyrite. The weight percentages of minerals (Table 3) were combined with TOC wt% and normalised to 100%. These minerals are grouped into granular minerals (including albite, calcite, dolomite, pyrite and quartz), clay minerals (including chlorite and muscovite) and organic matter in each sample for further analysis. Among the three gas-mature samples, L1 (high TOC, Lublin) has the highest content of organic matter, L2 (medium TOC, Lublin) has the highest clay mineral content and L3 (low TOC, Lublin) has the highest content of granular minerals (Table 3). Between the two high TOC samples, L1 (gas mature, Lublin) has less granular minerals, higher clay minerals and similar organic matter content compared with B1 (oil mature, Baltic).

Optical microscopy and SEM imaging reveal that all of the mudstone samples consist of variable sized (2–15 μm) mineral grains including quartz, calcite, dolomite and albite (Fig. 2). The granular minerals are embedded within a clay mineral-rich matrix composed of lamellar clay minerals including chlorite and muscovite. Amorphous organic matter particles scattered in the matrix vary in size from < 1 μm to > 100 μm. In some studied samples, bedding laminations ranging from a few microns to a few millimetres thick are formed of partially-oriented (parallel to bedding) clay minerals and organic matter particles (Fig. 2A–D). In particular, the high TOC L1 and B1 samples possess thick laminations (~5.0 mm), and partially-aligned clay minerals, with elongated organic matter particles present in the matrix (Fig. 2A and D). The medium TOC L2 sample has thin laminations (0.1–1.0 mm), and partially-aligned clay minerals with small organic matter particles scattered in the matrix (Fig. 2B). The low TOC L3 sample has no obvious lamination (Fig. 2C), and has sub-angular carbonate minerals (5–20 μm in size) and siliceous minerals (1–10 μm in size) within a clay-mineral rich matrix (Fig. 2E).

4.2. Organic matter

The nature, shape and size of organic matter in the Lublin and Baltic Basin samples vary considerably. The wide size-range of organic matter particles required quantification of morphological and topological parameters over several scales. The morphological characteristics of organic matter include the geometry and local thickness, and the topological parameters include connectivity and orientation. Due to the limits of resolution, individual organic matter components cannot be resolved at the mesoscale (R1) (Appendix Fig. 1). The geometry and orientation of organic matter particles can be resolved from the microscale (R2) (Fig. 3), and local thickness and connectivity can additionally be resolved at the sub-micron scale (R3) and nanoscales (R4 & R5) (Fig. 7, Appendix Fig. 2 and Fig. 10). The results of the above are outlined below.

4.2.1. Geometry

Observations from light microscopy, SEM and 3D FIB data indicate that organic matter particles take one of two forms: 1) large lamellar-shaped particles and 2) small spheroidal particles, (Figs. 2F, 3 and 4). Large lamellar organic matter particles were observed primarily in the organic-rich samples (TOC > 4%) and consist of organic matter horizontally aligned to bedding (Figs. 3 and 4A, C). These particles vary considerably in size (1–100 μm long, 0.5–2 μm thick) and appear to be associated with the clay mineral-rich matrix. Small spheroidal organic matter particles were observed in all samples and consist of spheroidal to ellipsoidal particles (5–20 μm diameter) and have no preferential alignment (Figs. 3 and 4A, B). In the low-TOC sample L3, small (0.5–2 μm), isolated organic matter particles were observed surrounded by granular mineral grains and clay minerals (Fig. 3C).

On the basis of ratio of length to width, spheroidal organic matter particles primarily have ratios below 3, while large lamellar organic matter particles have ratios over 3 and generally have a long axis > 30 μm (Fig. 4). Lamellar particles also generally have well-defined boundaries that are commonly parallel to sub-parallel to bedding and spherical particles are discrete with no preferred orientation. The

Table 3
XRD mineral compositions (corrected) and TOC concentration of samples.

		Quartz	Albite	Calcite	Dolomite	Pyrite	chlorite	Muscovite	TOC	Total
Weight percentages (%)	L1	34	12	2	1	1	19	22	9	100
	L2	32	12	3	4	1	14	30	4	100
	L3	31	13	2	12	1	15	25	1	100
	B1	31	10	11	1	1	9	27	10	100

Mixed phase		Granular minerals	Clay minerals	Organic	Total
Weight percentages (%)	L1	50	41	9	100
	L2	52	44	4	100
	L3	59	40	1	100
	B1	54	36	10	100

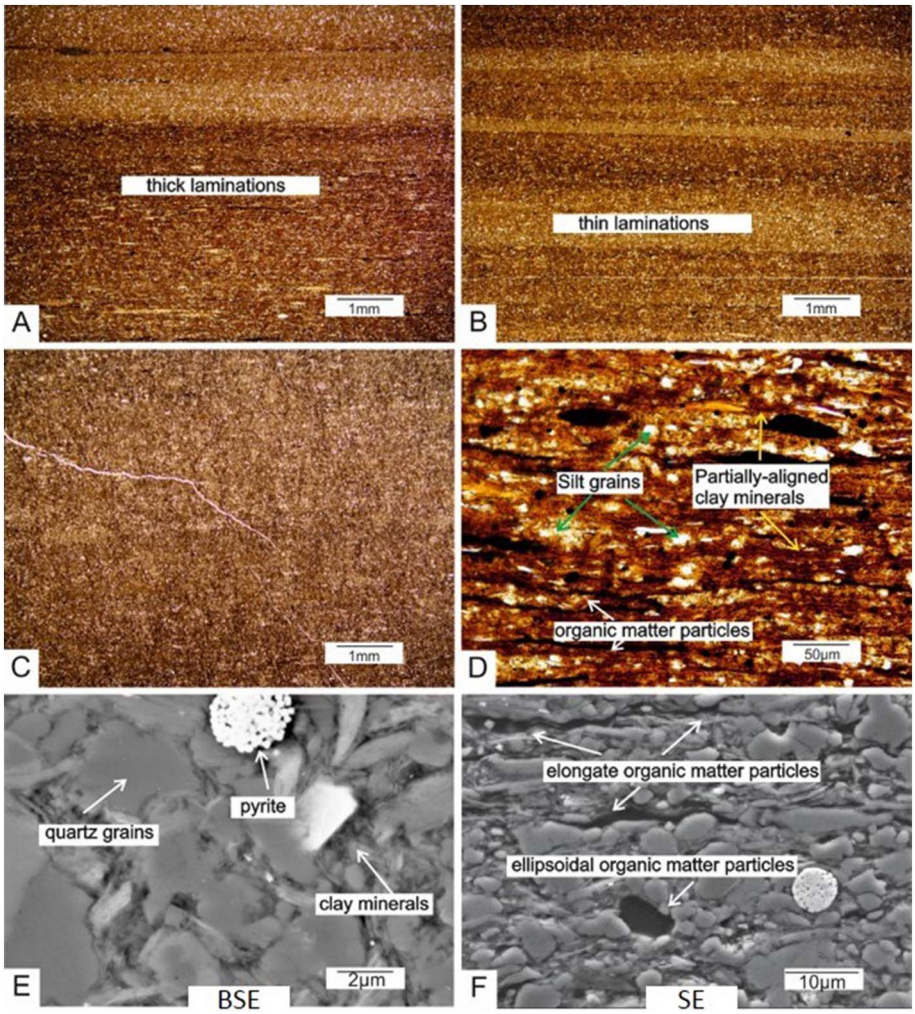

Fig. 2. Optical microscope and SEM images of three gas-mature samples in Lublin basin along TOC gradient and one oil-mature sample in Baltic basin with high TOC. A: thickly-laminated (~5 mm), high TOC sample, L1; B: thinly-laminated (0.1–1.0 mm), medium TOC sample, L2; C: unlaminated, low TOC sample, L3; D: an example of visible minerals and matrix under optical microscope, silt grains scattered with the matrix made up of partially-aligned clay minerals with organic matter particles, B1; E: an example of minerals and matrix under SEM, quartz grains dominate in the silt grains and clay minerals are partially-aligned, L3; F: both of elongate organic matter particles and isolated ellipsoidal organic matter are found in the matrix of high TOC sample, L1. BSE- backscattered electron image. SE-secondary electron image.

percentage of lamellar particles decreases with TOC while spherical particles show an inverse trend. In the L1 sample (high TOC), lamellar particles account for 75.1% of total organic particle volume (spherical particles 24.9%) (Fig. 2A). In the L2 sample (medium TOC), lamellar particles account for 40.5% of organic particle volume (spherical particles 59.5%) (Fig. 2B). In the L3 sample (low TOC), lamellar particles account for 6.9% of organic particle volume (spherical particles 93.1%) (Fig. 2C). In terms of particle frequency, lamellar organic particles are less common than spherical organic particles. Lamellar particles account for 32.4% of the individual organic particles in the L1 sample (spherical particles 68.6%). In the L2 sample they are less frequent accounting for 11.2% of the organic particles (spherical particles 88.8%). In the L3 sample the account for 1.7% of the total organic particles in measured (spherical particles 98.3%). With increasing TOC the frequency and total volume of lamellar organic particles increases. Lamellar organic matter also accounts for a significantly higher proportion of organic volume when compared to its frequency. Spheroidal organic matter exhibits the opposite trends of decreasing with TOC concentrations and having a small volume relative to its frequency.

4.2.2. Local thickness

Where lamellar organic matter pieces dominate, volume or diameter is not a sufficient descriptor of organic matter particles, and therefore organic matter thickness is considered to be more appropriate. At the R2 scale, the greatest local thickness occurs in the organic-rich sample (maximum value 42 μm in L1, Fig. 5A). Lower local thickness values are present in L2 and L3 samples with maximum sizes of 40 and 26 μm, respectively (Fig. 5A). Similarly, the L1 has maximum values of 22 μm thickness at R3 scale, while L2 and L3 have similar maximum values at 15 μm and 12 μm respectively (Fig. 5B). The absolute values of local thickness at R3 were relatively lower than R2 due to the limited field of view.

4.2.3. Connectivity

Organic matter connectivity increases with increasing TOC concentration (L3 < L2 < L1). At the scale R3, 78% of organic matter is connected in L1. No connected organic matter is found all through samples in L2 and L3 (Fig. 6). The majority of organic matter particles in sample L2 are distributed in the range of 0.2–2 μm, and sample L3 has relatively small sizes of organic matter particles, the majority of which are in the range of 0.06–0.7 μm. Lamellar organic matter particles in L1 at scale R4 were also analysed for connectivity, and 98.36% of organic matter in this volume was connected with the narrowest throat is only 0.2 μm although the images not presented here (Appendix Fig. 2).

4.3. Pore system

Quantification of the pore system can only be attempted at resolution R5 due to small pore sizes and the limits of resolution. Porosity, pore size distribution, pore types, morphological parameters and topological parameters of pores were measured and analysed based on imaging and laboratory measurements.

4.3.1. Porosity and pore size distribution

4.3.1.1. Porosity. Measured helium porosities (Table 4) demonstrate

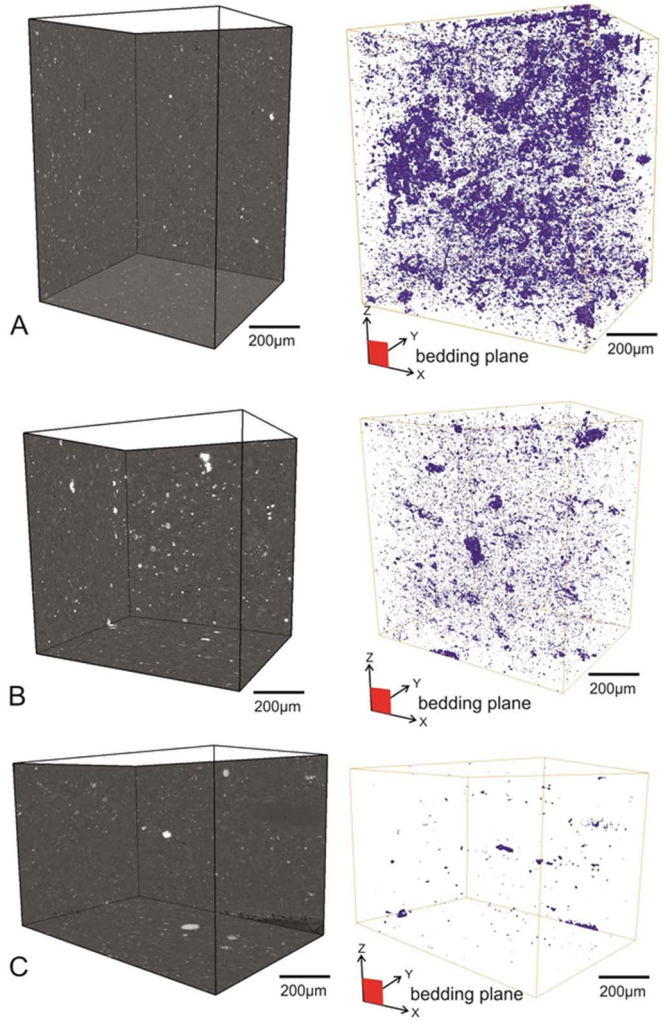

Fig. 3. Ortho slices and 3D rendering of organic matter geometry and distribution with TOC gradient at micro scale (R2). A: L1 sample, large lamellar organic matter particles and small spheroidal organic matter particles both observed; B: L2 sample, low numbers of large lamellar organic matter particles; C: L3 sample, dominated by and small spheroidal organic matter particles.

that total effective porosity does not seem to vary with organic matter or maturity with similarly low porosity in all the samples: L1 (2.3%), L2 (2.4%), L3 (2.0%) and B1 (2.4%). Porosity measured using nitrogen adsorption (Fig. 10) (which measures pores within the 2–300 nm size range) gives higher values: L1 (3.45%), L2 (4.11%), L3 (3.12%) and B1 (5.53%) (Table 4).

4.3.1.2. Pore size distribution. 3D images (FIB-SEM) have been used for the size distributions of pores above 20 nm, while pores below imaging resolution, with sizes between 2 and 20 nm, were identified from nitrogen sorption data. The combined data for pore-size distributions are shown in Fig. 7.

For invisible pores under 20 nm, these four samples all have two peaks at 3 nm and 8–10 nm in pore size distribution according to the BJH results from nitrogen adsorption (Fig. 7). Imaging results of visible pores above 20 nm show that the majority of pore sizes in all samples are distributed from 0.02 to 3 μm, with bimodality at 0.04–0.05 μm and 0.01–0.2 μm, and a minor peak around 1–2 μm (Fig. 7).

4.3.2. Pore types

All visible pores are categorized into two groups based on their occurrence: organic matter-associated pores and mineral-associated pores. Both groups can be further classified based on component phase association into: 1) intra-organic matter pores (IntraO), 2) organic interface pores (InterO), 3) inter-mineral pores (InterM) and 4) intra-mineral pores (IntraM) (Ma et al., 2016).

IntraO pores are completely bounded by organic matter. These pores have spherical or ellipsoidal geometries, with some examples having a linear serial distribution (Figs. 8A and B, and 9). This type of pore occasionally occurs in the lamellar and elongate organic matter types in gas-mature samples from the Lublin Basin and is rare in spherical organic matter particles from Lublin Basin or in the oil-mature Baltic Basin sample. IntraO pores are observed to vary with organic concentration and maturity (Fig. 9). This type occupies 20% of total porosity in high TOC gas-mature sample (L1) but only 2% and 1% in medium and low TOC samples (L2 and L3) (Table 4 and Fig. 9A–C). No IntraO pores were observed in the oil-mature Baltic Basin sample.

InterO pores occur at the interface of organic matter and other minerals, particularly between organic matter and clay minerals. These pores are found in all samples. They often have an irregular, crack-like or elongate morphology with a large size range, 0.02 μm to 2 μm (Figs. 8C and D, 9). Organic interface pores account for the second largest portion of pores specifically, 39% for L1, 34% for L2 and 3% for L3 (Table 4 and Fig. 9A–C). The overly large organic interface pore in B1 is rare in observation and speculated to be artificial therefore not considered in the further comparison (Fig. 9D).

InterM pores are elongate, lenticular or spheroid in geometry and surrounded by clay minerals, quartz, calcite, dolomite and other trace minerals. Pores range in size from 0.04 to 1 μm (Figs. 8E and F, 9). Pores between phyllosilicate minerals, especially muscovite and chlorite, are wedge-like or elongate while pores around other silicate grains or carbonate grains are lenticular or irregular. Inter-mineral pores account for the largest portions for each samples, specifically, 40% for L1, 63% for L2, 94% for L3 and 21% for B1 (Table 4 and Fig. 9).

IntraO pores are present within individual mineral particles. They are often present as angular polygons or irregular spheres within crystals of calcite, dolomite, and framboidal pyrite with a size range of 0.03–0.3 μm (Figs. 8G and H, 9). Pores within carbonate grains generally have a round or polygonal shape. Pores in pyrite framboids are irregularly shaped. L1 and L2 have the same volume fraction of IntraM pores, 1%, while L3 and B1 have the similar volume fractions, 2%,

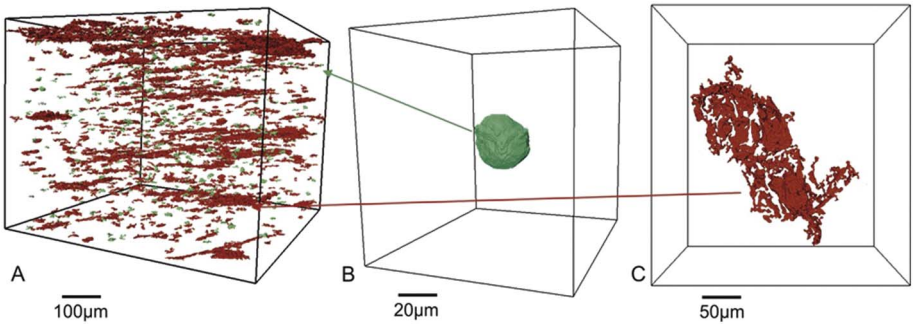

Fig. 4. The two organic matter particles types in L1 at R2 scale. Small spheroidal organic matter pieces (green in A and B) and large lamellar (red in A and C) organic matter particles. (For interpretation of the references to colour in this figure legend, the reader is referred to the web version of this article.)

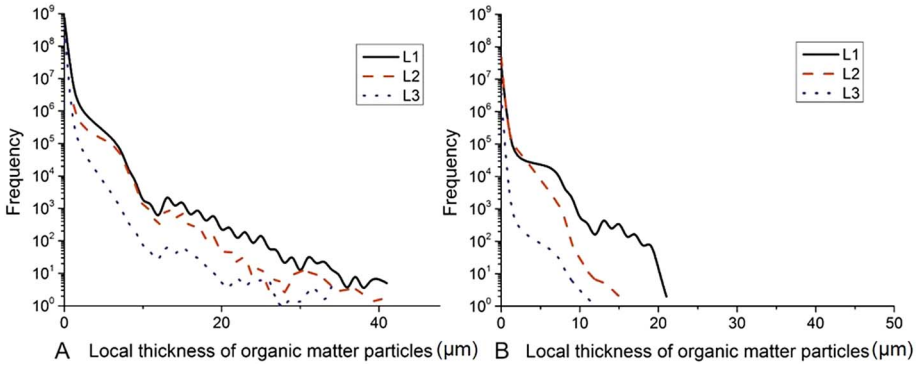

Fig. 5. Distribution of organic matter local thickness at micro scale R2 (A) and sub-micron scale R3 (B).

correspondingly (Table 4 and Fig. 9).

Pores > 0.1 μm in equivalent diameter are dominated by inter-particle pores (InterO and InterM) (Fig. 10A), with two peaks at 0.04 μm and 0.2 μm. While intra-particle pores (IntraO and IntraM) of these samples have relative small sizes, with major peaks at around 0.04–0.08 μm.

Pore volumes are presented as fractions which are then binned by equivalent diameter. Pores with diameters of 0.1–0.2 μm have the largest volume fraction of all pore types (Fig. 10B). Corresponds to the size distribution, the pore volume distributions of inter-particle pores show peaks at 0.2 μm, while those of the intra-particles pores present increasing trends with pore sizes. Specifically, InterM pores have higher volumes for each bin, followed by InterO pores and IntraO pores, while IntraM pores only occupy a small portion (Fig. 10B).

4.3.3. Geometry of pores

Inter-particle pores have more elongate shapes than intra-particle pores on the basis of shape factor distribution, which is quantified by the ratio of length and width (Fig. 10C). The elongation factor of IntraO pores peaks at 1–2 (length/width), indicating the relative spherical geometries (Fig. 10C). InterO pores have relative elongate shapes than IntraO pores, peaking at 1-3 for L1-3 samples and 4 for B1 sample (Fig. 10C). In term of InterM pores. B1 has a peak at around 4, while the other three samples peak at 1-2 (Fig. 10C). The dominant elongation facto of IntraM pores is between 1 and 3 (Fig. 10C).

5. Discussion

We discuss the data presented above with the view of assessing the controls on pore types and distribution in these rocks, together with the relationship between organic matter content and connectivity of organic matter and pore networks.

5.1. Organic matter variation

Organic matter provides the hydrocarbon source for shale reservoirs, and the geometry and network of organic matter impacts the physical and chemical properties of shale (Curtis et al., 2014; Romero-Sarmiento et al., 2013). Previous authors have identified isolated organic matter- associated pore systems and suggested diffusive transport through organic matter particles might be possible (Javadpour et al., 2007; Ma et al., 2016; Thomas and Clouse, 1990; Yuan et al., 2014).

The two geometries of organic matter particles identified in this study (small spheroidal and large lamellar) we interpret to reflect diverse organic compositions (the different maceral types liptinite, vitrinite, inertinite, solid bitumen) in individual particles (Behar and Vandenbroucke, 1987; Tissot et al., 1974). The lamellar organic particles may be semifusinite (inertinite), and the small spheroidal or ellipsoid particles may be algal bodies in liptinites or woody debris in intertinite (Tissot et al., 1974).

Organic matter connectivity appears to be influenced by the organic matter concentration. Only the R2 and R3 scales can be considered for organic matter network analysis as the sample volumes at R4 and R5 scales are not sufficiently representative. The L1 sample (TOC 9%, gas-mature), with an organic matter volume of 13 vol%, (6 wt%), does not show an inter-connected organic network at R2. While in the B1 sample (TOC 10%, oil-mature) at R2, the connectivity of organic matter is over 80% and organic matter concentration is 36 vol% (18 wt%). The difference in connectivity suggests organic matter will become an inter-connected network when organic matter content in selected region increases to a value between 6 and 18 wt%.

Organic matter connectivity can be also influenced by the physical and chemical properties, for example, the geometry and compositions of organic matter. Lamellar organic matter (length: width ratio > 3) is more connected than spheroidal organic matter (length: width ratio < 3) where the volume is the same.

5.2. Pore system variation

In the studied samples, there are two major pore types associated with organic matter: IntraO and InterO pores. These organic matter-related pores have been identified by other scholars (Milliken et al.,

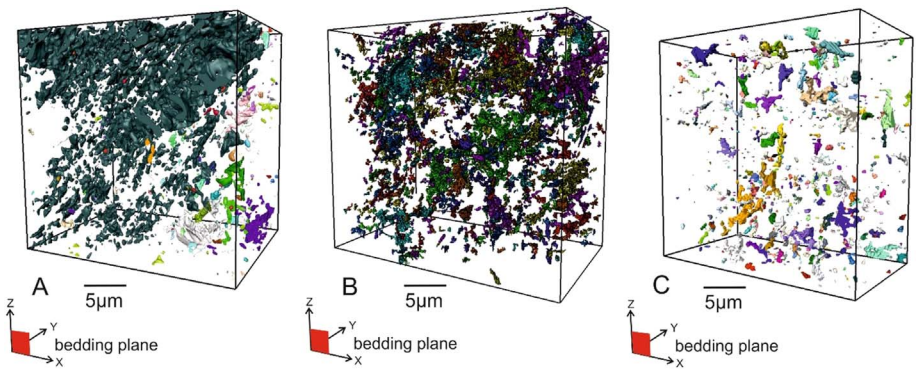

Fig. 6. Segmented organic matter pieces at sub-micron scale (R3), colours refer to separate organic matter particles. A: 78% of organic matter is connected in sample L1; B: separated organic matter particles and majority of them distribute in the range of 0.2–2 μm in sample L2; C: separated organic matter particles and majority of them distribute in the range of 0.06–0.7 μm in sample L3.

Table 4
Quantification of organic matter, minerals and pores from laboratory measurements and 3D images.

Measurement			L1	L2	L3	B1
Sample depth (m)			2969	2970	2899	1938
Organic petrology	TOC (wt%)		9	4	1	10
	Transferred TOC (vol%)		18	8	2	20
	R_O (%)		2.2	2.2	2.2	0.8
XRD	Granular minerals (wt%)		50.2	51.8	59.1	53.4
	Clay minerals (wt%)		40.8	44.2	39.9	35.6
BET (nitrogen sorption)	BET surface area (m^2/g)		2.71	3.59	2.46	4.24
	BJH Total pore volume (%)		3.45	4.11	3.12	5.53
	Helium porosity (dried, %)		2.3	2.4	2.0	2.4
3D images	R2	Organic matter volume fraction (vol%)	13.25	4.51	1.69	35.71
		Organic matter connectivity (%)	0	0	0	95
		Organic matter maximum thickness(μm)	45	42	26	112
	R3	Organic matter volume fraction (vol%)	8.95	3.08	2.67	27.97
		Organic matter connectivity (%)	78	0	0	96
		Organic matter maximum thickness	21	15	12	30
	R4	Organic matter volume fraction (vol%)	29.13	/	/	/
		Organic matter connectivity (%)	98.36	/	/	/
	R5	Organic matter (vol%)	62.3	14.84	42.5	49.8
		Pore volume (μm^3)	9.14×10^{-3}	9.53×10^{-4}	$7. \times 10^{-4}$	7.84×10^{-3}
		IntraO pores (vol%)	0.40	0.01	0.02	0.00
		InterO pores (vol%)	0.49	0.35	0.02	0.77
		InterM pores (vol%)	0.10	0.63	0.94	0.21
		IntraM pores (vol%)	0.01	0.01	0.02	0.02

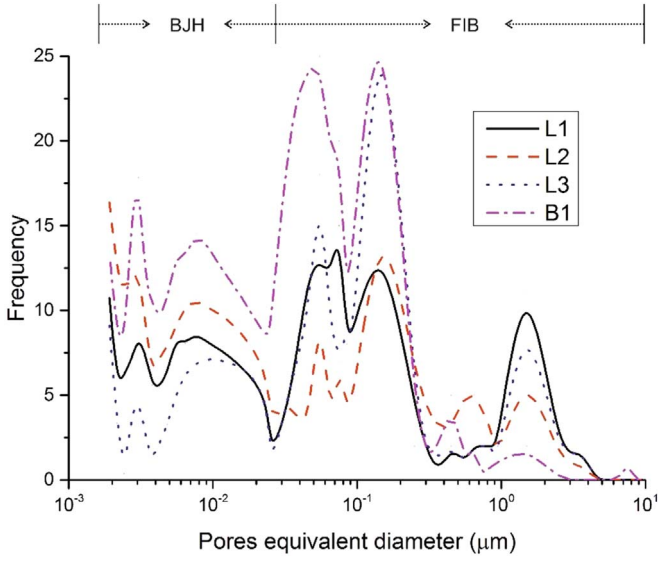

Fig. 7. Combined pore sizes distributions from N_2 sorption experiment (based on BJH theory) and FIB images.

2013; Ross and Bustin, 2009) as potentially important in both the storage and flow of hydrocarbons. Organic matter hosts a significant pore system in many shale plays (Klaver et al., 2015; Milliken et al., 2013), and organic matter concentration, maturity and compositions may therefore be important factors in porosity distribution and fluid flow in shale reservoirs.

Comparison between two gas-mature samples L3 and L1 shows that the latter has 8% more TOC, 8% less granular minerals and nearly an equivalent content of clay minerals. L1 has higher organic matter-related porosity and also higher total porosity than L3 which suggests organic matter can have a significant contribution to porosity independent from variations in clay mineral-related porosity.

In the gas-mature Lublin Basin samples, a high concentration of IntraO and InterO pores were observed. The number and volume of these two organic matter-related pores are lowest in the low TOC sample (L3). In contrast to this pore system, rare IntraO pores are found in the oil-mature Baltic samples. Thermal maturity is therefore a possible control for this difference in organic matter-related pores (Curtis et al., 2012a).

The elongate, crack-like pores are present at the interface of organic matter and minerals (Figs. 8C–D and 9), which may have generated from the fluid pressure during oil generation in the first decomposition stage of kerogen to oil (Sondergeld et al., 2013). Some of these pores may have formed due to shrinkage of the organic matter post-coring (Loucks et al., 2009), for example, the large piece of connected yellow InterM pore in B1 (Fig. 9D). Therefore the high BET surface area and high porosity between 2 and 300 nm in the B1 sample may have been caused by a proportion of the large crack-like pores between organic matter and other minerals. It may also partly be caused by the less compaction in B1 as the depth of B1 is over 1 km less than oil mature samples (Table 4). The spherical IntraO pores in gas-mature samples (Ro, 2.2%) of the Lublin Basin may be generated during secondary decomposition of kerogen to gas (Ro, 1.1–1.3%) and the secondary cracking of oil to gas (Ro, 2.0%) stages (Bernard and Horsfield, 2014; Jarvie et al., 2007).

Not all organic matter particles have similar features within the pore system, although they have similar mineral composition, diagenesis and thermal history (Loucks et al., 2009; Passey et al., 2010). In a proportion of the lamellar organic matter particles, there are many IntraO pores linearly distributed. In spheroidal organic matter, IntraO pores could not be resolved. Although lamellar and spheroidal organic matter experienced the same burial and thermal histories, only one developed a resolvable pore system. This may indicate that differences in organic matter types could control organic matter-related porosity.

Among the three gas-mature samples, the relatively high frequency and volume fraction of InterM pores associated with clay minerals observed in 2D SEM and 3D FIB images (Fig. 10 and Table 4), as well as the higher helium porosity and BJH porosity in the clay-rich L2 sample (Fig. 7 and Table 4) may indicate that clay mineral content rather than organic matter concentration is the primary control on total pore frequency and volume.

InterM pores associated with clay minerals have an elongate wedge-like geometry and tend to parallel the bedding plane (Figs. 7 and 8). The preservation of InterM pores is likely to be controlled by both physical compaction and chemical cementation during burial and diagenesis. More elongate pore geometries and greater horizontal alignment of InterM pores (green in Figs. 9 and 10) in Lublin Basin samples compared to Baltic Basin samples may be due to deeper burial resulting

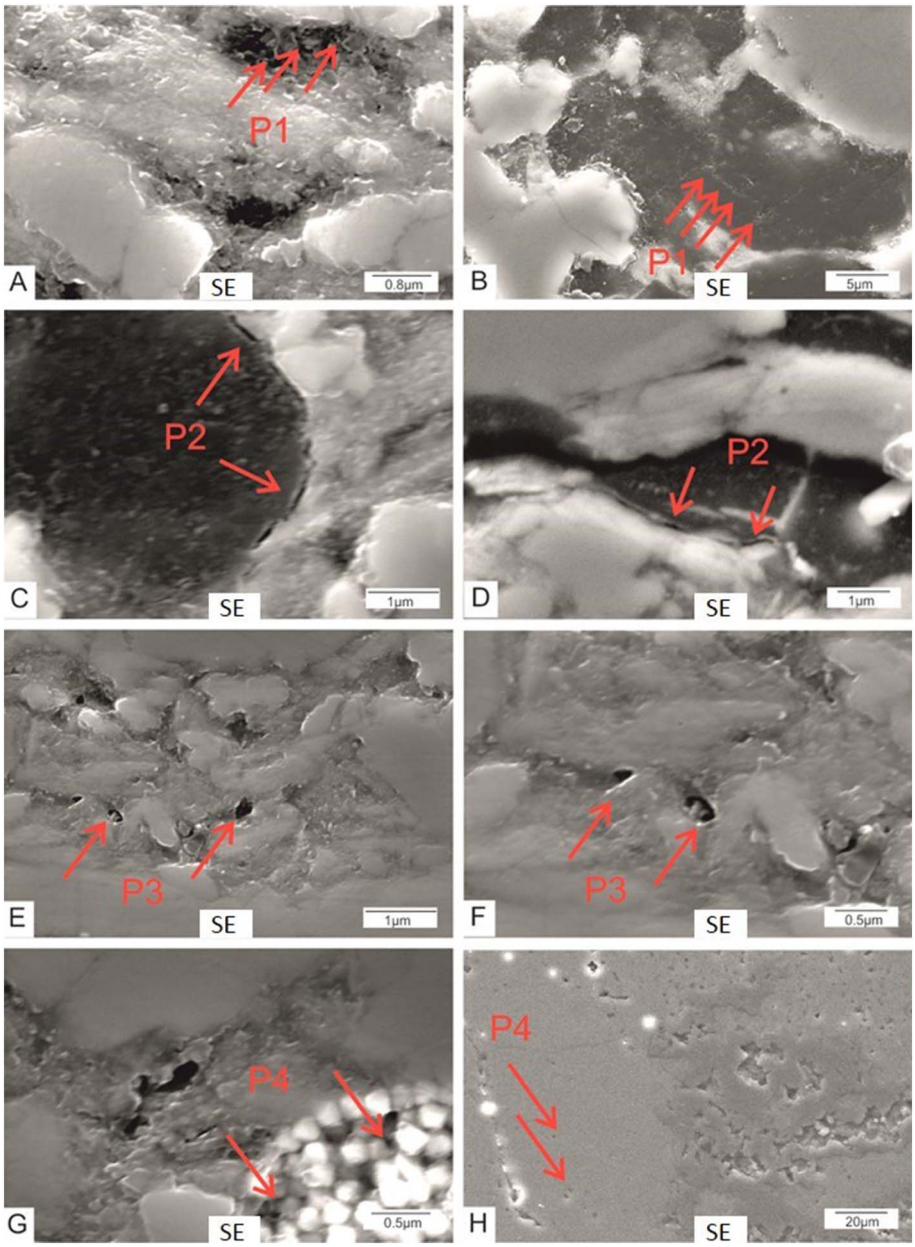

Fig. 8. SEM images of pore types. A: IntraO pores spreading in organic matter particles, B: small and spherical IntraO pores arrange in line, C–D: crack-like and intermittent InterO pores at the interface of organic matter particles and other minerals such as quartz and clay minerals, E–F: InterM pores lying between minerals, G: irregular-shape IntraM pores within pyrite framboids, H: regular-shape IntraM pores within carbonate minerals such as calcite. BSE- backscattered electron image. SE-secondary electron image.

in greater compaction of clay minerals. This greater alignment may result in higher horizontal permeability and lower vertical permeability because of linear distribution of pores post-compaction.

6. Conclusions

(1) Multi-scale observations were made on porosity and organic-matter size, geometry and distribution, for selected samples of Silurian shales from the Lublin and Baltic Basins of Poland and Lithuania, respectively. 3D and 2D datasets were collected using a combination of XCT, FIB-SEM and standard optical and electron microscopy over three scales (2 orders of magnitude, pixel sizes from 0.5 μm to 5 nm). Physical and chemical data were collected through TOC, XRD, and helium porosity and nitrogen sorption measurements.

(2) The data indicate that both organic matter geometry and concentration control the organic matter network. Two organic matter types are distinguishable in 3D imaging data sets, (i) small spheroidal and (ii) large lamellar particles. The latter contribute more in connectivity in case of the same volume. Organic matter becomes an interconnected network when organic matter content in selected region increases to a value between 6 and 18 wt% (a maximum of 18 wt% was observed in our samples).

(3) Four different pore types have been recognised in the samples studied and, in decreasing order of frequency and total volume, are: inter-mineral pores, organic interface pores, intra-organic pores and intra-mineral pores.

(4) The major control on porosity within these shales is not organic matter content, but rather clay mineral content. Increasing clay mineral content is associated with higher porosity. The higher frequency of inter-mineral pores explains the positive relationship between porosity and clay mineral contents in this sample set.

(5) Intra-organic pores are only observed in the gas mature samples, consistent with previous studies suggesting these pores to be the result of porosity generation during secondary kerogen decomposition and oil cracking to gas.

(6) This research highlights the power on integrating multi-scale 3D and 2D observations on understanding the reservoir characteristics, and the controls on variability, in these complex porous media.

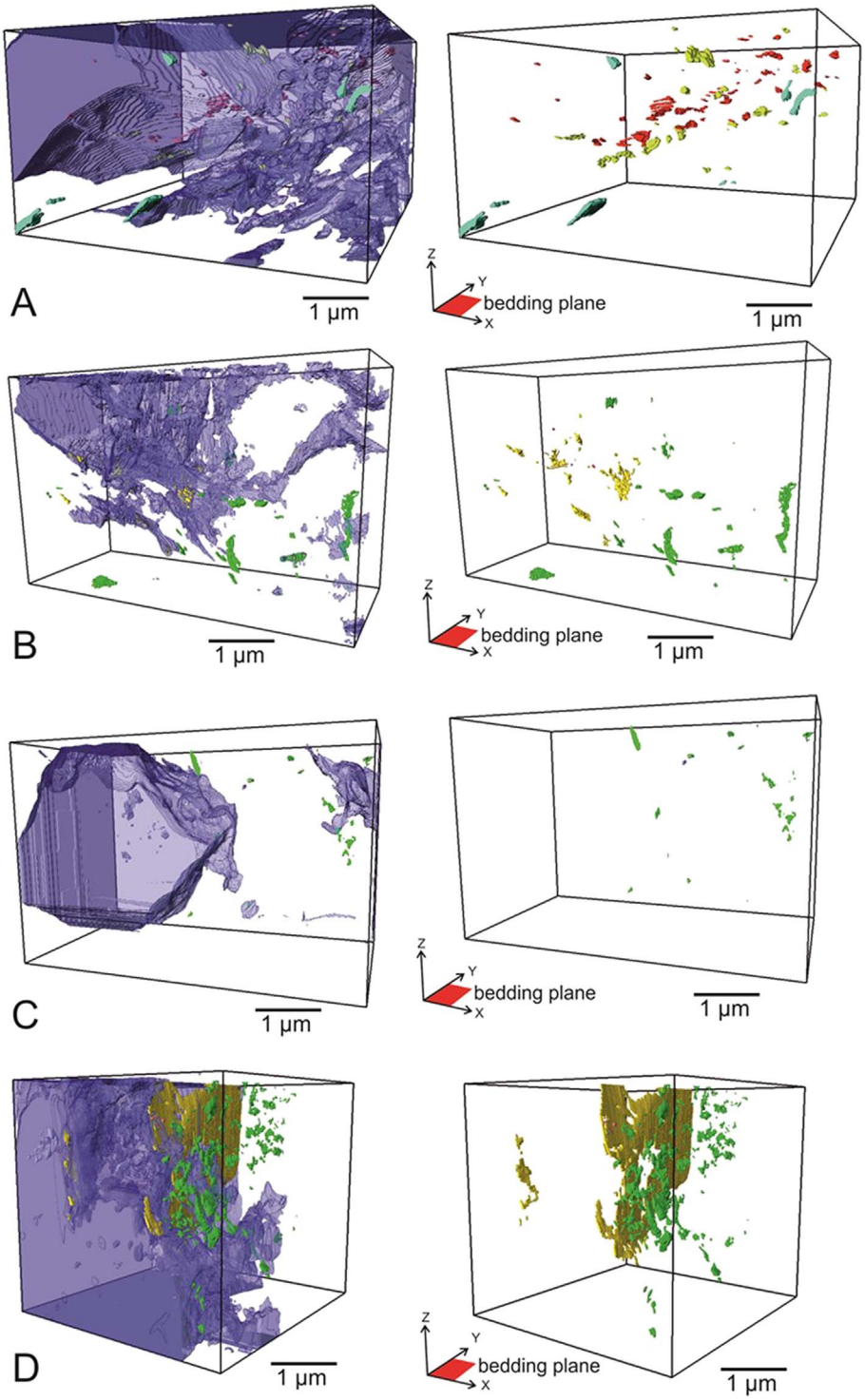

Fig. 9. 3D renderings of segmented pores and organic matter in all samples, (left - organic matter and pores, right - pores). A: L1, B: L2, C: L3 and D: B1, transparent blue: organic matter, red: IntraO pores, yellow: InterO pores, green: InterM pores, pink: IntraM pores. (For interpretation of the references to colour in this figure legend, the reader is referred to the web version of this article.)

Acknowledgements

The authors would like to acknowledge the Chevron for providing samples, The Henry Mosley X-ray Imaging Facility, The Diamond Manchester Collaboration, and The Electron Microscopy Centre, University of Manchester for providing facilities. Thanks to colleagues in Research Complex at Harwell and Henry Mosley X-ray Imaging facility for help with image acquisition and analysis. LM wishes to acknowledge the China Scholarship Council for PhD support. This work was supported financially by UK-NERC (NE/M001458/1), the European Union's Horizon 2020 716 Research and Innovation Programme under the ShaleXenvironmenT Project (grant no. 640979), and Mudstone and Shale Research Consortium constituted by Shell (formerly BG Group), Chevron, and Schlumberger. The synchrotron imaging was performed at the Diamond-Manchester Branchline of Diamond Light Source (DLS), Beamtime MT4022.

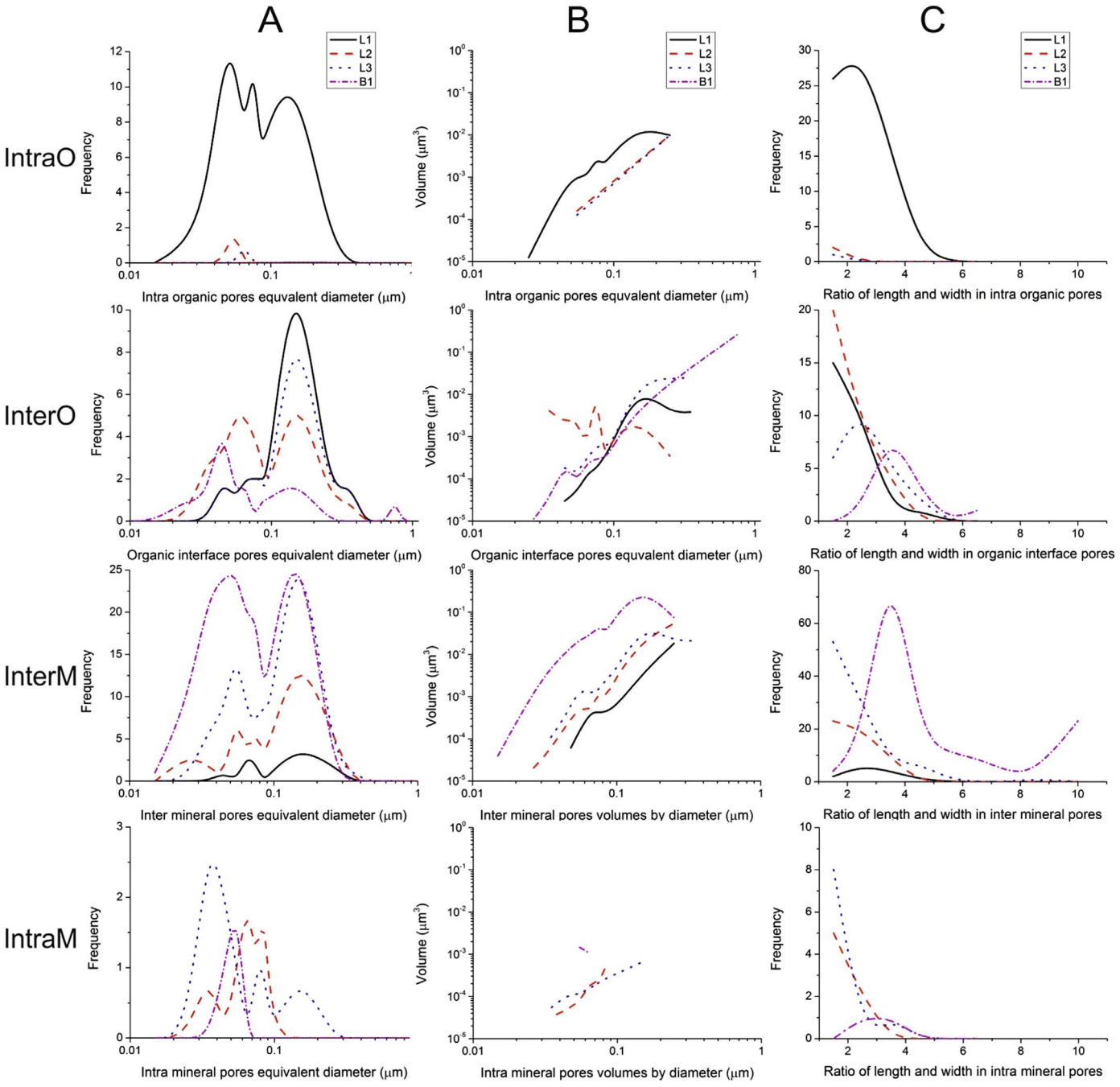

Fig. 10. Pore analysis diagrams on pore types from 3D imaging data. Columns: A pore size, B pore volume, C pore shape (length/width), rows: P1 IntraO pores, P2 InterO pores, P3 InterM pores and P4 IntraM pores. (For interpretation of the references to colour in this figure legend, the reader is referred to the web version of this article.)

Appendix A

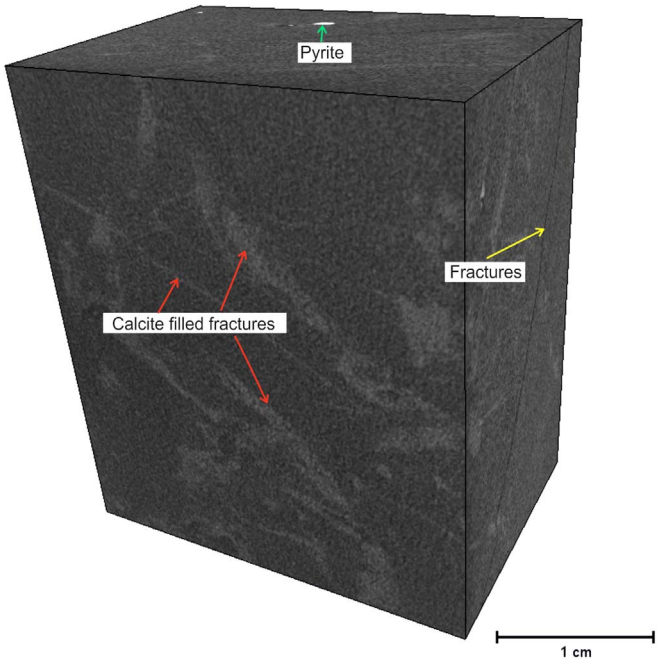

Appendix Fig. 1. Ortho slices of 3D XCT data in L1 sample at macroscale (R1), showing calcite filled fractures, fractures and pyrite but not organic matter particles.

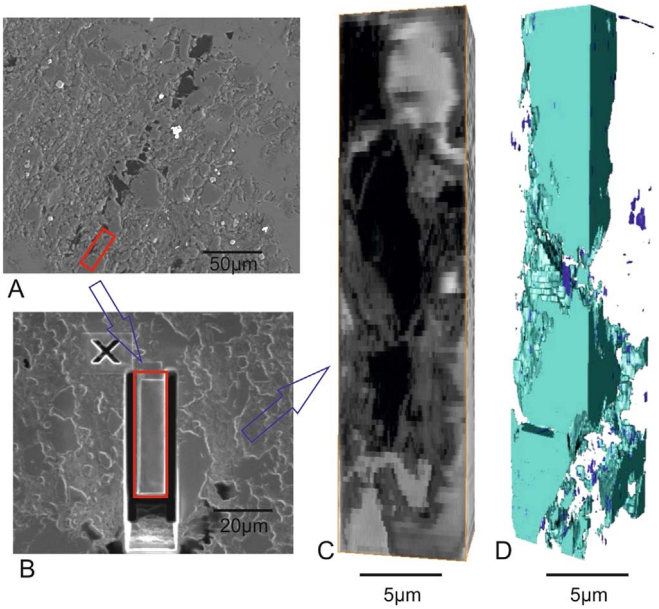

Appendix Fig. 2. SEM and FIB images showing organic connectivity at low-resolution nanoscale (R4). A intermittent organic matter distribute in line. B FIB milling position showing in secondary electron SEM. C the organic matter pieces shown in image slices. D 98% of organic matter in the same area is connected, shown in FIB, Green- connected organic matter, blue- isolated organic matter. (For interpretation of the references to colour in this figure legend, the reader is referred to the web version of this article.)

Reference

Ambrose, R.J., Hartman, R.C., Diaz-Campos, M., Akkutlu, Y., Sondergeld, C.H., 2010. New pore-scale considerations for shale gas in place calculations. In: Petroleum Engineers Unconventional Gas Conference. Society of Petroleum Engineers, Pittsburgh, Pennsylvania.

Bai, B., Elgmati, M., Zhang, H., Wei, M., 2013. Rock characterization of Fayetteville shale gas plays. Fuel 105, 645–652.

Barrett, E.P., Joyner, L.G., Halenda, P.P., 1951. The determination of pore volume and area distributions in porous substances. I. Computations from nitrogen isotherms. J. Am. Chem. Soc. 73, 373–380.

Behar, F., Vandenbroucke, M., 1987. Chemical modelling of kerogens. Org. Geochem. 11, 15–24.

Bernard, S., Horsfield, B., 2014. Thermal maturation of gas shale systems. Annu. Rev. Earth Planet. Sci. 42, 635–651.

Bocangel, W., Sondergeld, C., Rai, C., 2013. Acoustic mapping and characterization of organic matter in shales. In: SPE Annual Technical Conference and Exhibition. Society of Petroleum Engineers.

Britt, L., 2012. Fracture stimulation fundamentals. J. Nat. Gas Sci. Eng. 8, 34–51.

Brownrigg, D., 1984. The weighted median filter. Commun. ACM 27, 807–818.

Brunauer, S., Emmett, P.H., Teller, E., 1938. Adsorption of gases in multimolecular layers. J. Am. Chem. Soc. 60, 309–319.

Buades, A., Coll, B., Morel, J.-M., 2005. A non-local algorithm for image denoising. In: Computer Vision and Pattern Recognition, 2005. CVPR 2005. IEEE Computer Society Conference on. IEEE, pp. 60–65.

Clarkson, C.R., Wood, J., Burgis, S., Aquino, S., Freeman, M., 2012. Nanopore-structure analysis and permeability predictions for a tight gas siltstone reservoir by use of low-

pressure adsorption and mercury-intrusion techniques. SPE Reserv. Eval. Eng. 15, 648–661.
Curtis, M., Ambrose, R., Sondergeld, C., 2010. Structural characterization of gas shales on the micro-and nano-scales. In: Canadian Unconventional Resources and International Petroleum Conference.
Curtis, M.E., Ambrose, R.J., Sondergeld, C.H., Rai, C.S., 2011. Investigation of the relationship between organic porosity and thermal maturity in the Marcellus Shale. In: North American Unconventional Gas Conference and Exhibition. Society of Petroleum Engineers.
Curtis, M.E., Cardott, B.J., Sondergeld, C.H., Rai, C.S., 2012a. Development of organic porosity in the Woodford Shale with increasing thermal maturity. Int. J. Coal Geol. 103, 26–31.
Curtis, M.E., Sondergeld, C.H., Ambrose, R.J., Rai, C.S., 2012b. Microstructural investigation of gas shales in two and three dimensions using nanometer-scale resolution imaging. AAPG Bull. 96, 665–677.
Curtis, M.E., Goergen, E., Jernigen, J., Sondergeld, C.H., Rai, C.S., 2014. High-resolution mapping of the distribution and connectivity of organic matter in Shales. In: SPE Annual Technical Conference and Exhibition. Society of Petroleum Engineers.
EIA, 2011. World shale gas resources: an initial assessment of 14 regions outside the United States. US Department of Energy.
EIA, U., 2013. Annual energy outlook 2013, in: US Energy Information Administration (Ed.), (Washington, DC).
Ghous, A., Knackstedt, M.A., Arns, C.H., Sheppard, A., Kumar, M., Sok, R., Senden, T., Latham, S., Jones, A.C., Averdunk, H., Pinczewski, W.V., 2008. 3D imaging of reservoir core at multiple scales: correlations to petrophysical properties and pore scale fluid distributions. In: International Petroleum Technology Conference, (Kuala Lumpur, Malaysia).
Heath, J.E., Dewers, T.A., McPherson, B.J.O.L., Petrusak, R., Chidsey, T.C., Rinehart, A.J., Mozley, P.S., 2011. Pore networks in continental and marine mudstones: characteristics and controls on sealing behavior. Geosphere 7, 429–454.
Hsieh, J., 2009. Computed Tomography: Principles, Design, Artifacts, and Recent Advances. SPIE, Bellingham.
Jarvie, D.M., Hill, R.J., Ruble, T.E., Pollastro, R.M., 2007. Unconventional shale-gas systems: the Mississippian Barnett Shale of north-central Texas as one model for thermogenic shale-gas assessment. AAPG Bull. 91, 475–499.
Javadpour, F., Fisher, D., Unsworth, M., 2007. Nanoscale gas flow in shale gas sediments. J. Can. Pet. Technol. 46, 55–61.
Jędrzejczyk, A., Rychlicki, S., Stopa, J., 2014. The characteristics of perspective areas of non-conventional oil accumulations in Poland. AGH Drill. Oil Gas 31.
Kanopoulos, N., Vasanthavada, N., Baker, R.L., 1988. Design of an image edge detection filter using the Sobel operator. IEEE J. Solid-State Circuits 23, 358–367.
Karcz, P.a., Janas, M., Dyrka, I., 2013. Polish shale gas deposits in relation to selected shale gas prospective areas of Central and Eastern Europe. Prz. Geol. 61.
Kelly, S., El-Sobky, H., Torres-Verdín, C., Balhoff, M.T., 2016. Assessing the utility of FIB-SEM images for shale digital rock physics. Adv. Water Resour. 95, 302–316.
Ketcham, R.A., Carlson, W.D., 2001. Acquisition, optimization and interpretation of X-ray computed tomographic imagery: applications to the geosciences. Comput. Geosci. 27, 381–400.
Klaver, J., Desbois, G., Littke, R., Urai, J.L., 2015. BIB-SEM characterization of pore space morphology and distribution in postmature to overmature samples from the Haynesville and Bossier Shales. Mar. Pet. Geol. 59, 451–466.
Korfiatis, P., Skiadopoulos, S., Sakellaropoulos, P., Kalogeropoulou, C., Costaridou, L., 2007. Combining 2D wavelet edge highlighting and 3D thresholding for lung segmentation in thin-slice CT. Br. J. Radiol. 80, 996–1004.
Kuila, U., Prasad, M., Derkowski, A., McCarty, D.K., 2012. Compositional controls on mudrock pore-size distribution: an example from Niobrara formation. In: SPE Annual Technical Conference and Exhibition. Society of Petroleum Engineers, San Antonio, Texas, USA.
Labani, M.M., Rezaee, R., Saeedi, A., Al Hinai, A., 2013. Evaluation of pore size spectrum of gas shale reservoirs using low pressure nitrogen adsorption, gas expansion and mercury porosimetry: a case study from the Perth and Canning Basins, Western Australia. J. Pet. Sci. Eng. 112, 7–16.
Landis, E.N., Keane, D.T., 2010. X-ray microtomography. Mater. Charact. 61, 1305–1316.
Liu, X., Xiong, J., Liang, L., 2015. Investigation of pore structure and fractal characteristics of organic-rich Yanchang formation shale in central China by nitrogen adsorption/desorption analysis. J. Nat. Gas Sci. Eng. 22, 62–72.
Long, H., Swennen, R., Foubert, A., Dierick, M., Jacobs, P., 2009. 3D quantification of mineral components and porosity distribution in Westphalian C sandstone by microfocus X-ray computed tomography. Sediment. Geol. 220, 116–125.
Loucks, R.G., Reed, R.M., Ruppel, S.C., Jarvie, D.M., 2009. Morphology, genesis, and distribution of nanometer-scale pores in siliceous mudstones of the Mississippian Barnett Shale. J. Sediment. Res. 79, 848–861.
Loucks, R.G., Reed, R.M., Ruppel, S.C., Hammes, U., 2012. Spectrum of pore types and networks in mudrocks and a descriptive classification for matrix-related mudrock pores. AAPG Bull. 96, 1071–1098.
Ma, Y., Zhong, N., Li, D., Pan, Z., Cheng, L., Liu, K., 2015. Organic matter/clay mineral intergranular pores in the Lower Cambrian Lujiaping Shale in the north-eastern part of the upper Yangtze area, China: a possible microscopic mechanism for gas preservation. Int. J. Coal Geol. 137, 38–54.
Ma, L., Taylor, K.G., Lee, P.D., Dobson, K.J., Dowey, P.J., Courtois, L., 2016. Novel 3D centimetre-to nano-scale quantification of an organic-rich mudstone: the carboniferous Bowland Shale, Northern England. Mar. Pet. Geol. 72, 193–205.
Ma, L., Fauchille, A.-L., Dowey, P.J., Pilz, F.F., Courtois, L., Taylor, K.G., Lee, P.D., 2017. Correlative multi-scale imaging of shales: a review and future perspectives. Geol. Soc. Lond., Spec. Publ. 454, SP454. 411.
Macbeth, C., Hajnasser, Y., Stephen, K., Gardiner, A., 2011. The effect of meso-seismic shale beds on the reservoir's stress sensitivity to seismic waves. Geophys. Prospect. 90–110.
Martínez, E., Engel, E., López-Iglesias, C., Mills, C.A., Planell, J., Samitier, J., 2008. Focused ion beam/scanning electron microscopy characterization of cell behavior on polymer micro-/nanopatterned substrates: a study of cell–substrate interactions. Micron 39, 111–116.
Milliken, K.L., Rudnicki, M., Awwiller, D.N., Zhang, T., 2013. Organic matter-hosted pore system, Marcellus Formation (Devonian), Pennsylvania. AAPG Bull. 97, 177–200.
Nagao, M., Matsuyama, T., 1979. Edge preserving smoothing. Comput. Graphics image Process. 9, 394–407.
Nawrocki, J., Poprawa, P., 2010. Development of trans-European Suture Zone in Poland: from Ediacaran rifting to early Palaeozoic accretion. Geol.Q. 50, 59–76.
Passey, Q.R., Bohacs, K.M., Esch, W.L., Klimentidis, R., Sinha, S., 2010. From oil-prone source rock to gas-producing shale reservoir - geologic and petrophysical characterization of unconventional shale-gas reservoirs. In: Engineers, S.O.P. (Ed.), CPS/SPE International Oil & Gas Conference and Exhibition in China, Beijing, China.
PGI, 2012. Assessment of Shale Gas and Shale Oil Resources of the Lower Paleozoic Baltic-Podlasie-Lublin Basin in Poland, First report. (Warsaw).
Poprawa, P., Šliaupa, S., Stephenson, R., 1999. Late Vendian–Early Palaeozoic tectonic evolution of the Baltic Basin: regional tectonic implications from subsidence analysis. Tectonophysics 314, 219–239.
Romero-Sarmiento, M.-F., Ducros, M., Carpentier, B., Lorant, F., Cacas, M.-C., Pegaz-Fiornet, S., Wolf, S., Rohais, S., Moretti, I., 2013. Quantitative evaluation of TOC, organic porosity and gas retention distribution in a gas shale play using petroleum system modeling: application to the Mississippian Barnett Shale. Mar. Pet. Geol. 45, 315–330.
Ross, D., Bustin, R.M., 2009. The importance of shale composition and pore structure upon gas storage potential of shale gas reservoirs. Mar. Pet. Geol. 26, 916–927.
Sakellariou, A., Sawkins, T.J., Senden, T.J., Arns, C.H., Limaye, A., Sheppard, A.P., Sok, R.M., Knackstedt, M.A., Pinczewski, W.V., Berge, L.I., Øren, P.-E., 2003. Micro-CT Facility for Imaging Reservoir Rocks at Pore Scales.
Sondergeld, C.H., Rai, C.S., Curtis, M.E., 2013. Relationship between organic shale microstructure and hydrocarbon generation. In: SPE Unconventional Resources Conference-USA. Society of Petroleum Engineers.
Stauber, M., Müller, R., 2008. Micro-computed tomography: a method for the non-destructive evaluation of the three-dimensional structure of biological specimens. Osteoporosis: Methods and Protocolspp. 273–292.
Thomas, M.M., Clouse, J.A., 1990. Primary migration by diffusion through kerogen: II. Hydrocarbon diffusivities in kerogen. Geochim. Cosmochim. Acta 54, 2781–2792.
Tissot, B., Durand, B., Espitalie, J., Combaz, A., 1974. Influence of nature and diagenesis of organic matter in formation of petroleum. AAPG Bull. 58, 499–506.
Wang, F.P., Reed, R.M., 2009. Pore networks and fluid flow in gas shales. In: Society of Petroleum Engineers Annual Technical Conference and Exhibition, New Oleans, Louisiana.
Wellington, S., Vinegar, H., 1987. X-ray computerized tomography. J. Pet. Technol. 39, 885–898.
Yuan, W., Pan, Z., Li, X., Yang, Y., Zhao, C., Connell, L.D., Li, S., He, J., 2014. Experimental study and modelling of methane adsorption and diffusion in shale. Fuel 117 (Part A), 509–519.
Zdanaviciute, O., Lazauskiene, J., 2007. The petroleum potential of the Silurian succession in Lithuania. J. Pet. Geol. 30, 325–337.
Zhang, S., Klimentidis, R.E., Barthelemy, P., 2011. Porosity and permeability analysis on nanoscale fib-sem 3d imaging of shale rock. In: International Symposium of the Society of Core Analysts, Austin, Texas, USA.